ACS NANO

www.acsnano.org

ARTICLE

On-the-Fly Nonadiabatic Dynamics Simulations of Single-Walled Carbon Nanotubes with Covalent Defects

Braden M. Weight, Andrew E. Sifain, Brendan J. Gifford, Han Htoon, and Sergei Tretiak*

Cite This: *ACS Nano* 2023, 17, 6208–6219

Read Online

ACCESS | Metrics & More | Article Recommendations | Supporting Information

ABSTRACT: Single-walled carbon nanotubes (SWCNTs) with covalent surface defects have been explored recently due to their promise for use in single-photon telecommunication emission and in spintronic applications. The all-atom dynamic evolution of electrostatically bound excitons (the primary electronic excitations) in these systems has only been loosely explored from a theoretical perspective due to the size limitations of these large systems (>500 atoms). In this work, we present computational modeling of nonradiative relaxation in a variety of SWCNT chiralities with single-defect functionalizations. Our excited-state dynamics modeling uses a trajectory surface hopping algorithm accounting for excitonic effects with a configuration interaction approach. We find a strong chirality and defect-composition dependence on the population relaxation (varying over 50−500 fs) between the primary nanotube band gap excitation E_{11} and the defect-associated, single-photon-emitting E_{11}* state. These simulations give direct insight into the relaxation between the band-edge states and the localized excitonic state, in competition with dynamic trapping/detrapping processes observed in experiment. Engineering fast population decay into the quasi-two-level subsystem with weak coupling to higher-energy states increases the effectiveness and controllability of these quantum light emitters.

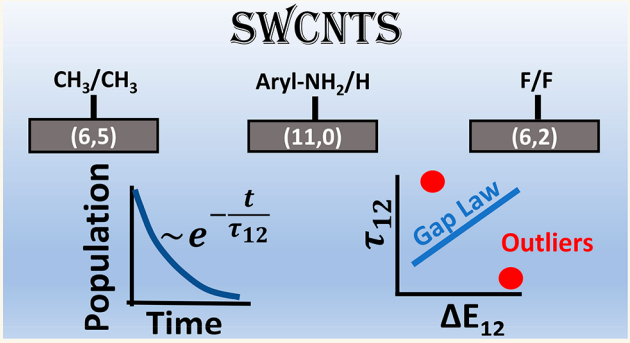

KEYWORDS: *single-walled carbon nanotubes, nonadiabatic excited-state dynamics, trajectory surface hopping, quantum defects, electron-vibrational relaxation*

Single-walled carbon nanotubes (SWCNTs) functionalized with a single[1−11] or multiple[12−15] sp^3-hybridized defects (each consisting of a covalent bond of two groups on a single carbon ring) are regarded as excellent sources of single photons at room temperature.[4,16,17] This makes them useful for applications in quantum circuits as well as in telecommunications[16] and other technologies relying on highly tunable single-photon emission. Much recent theoretical work has been done exploring the structure−property relationships in these systems from the point of view of the Condon geometry.[1−3,7,10,12,18] However, control over the dynamic processes following electronic excitation has only loosely been discussed from the theoretical side.[19−25] A better understanding of these processes, such as carrier trapping and detrapping,[5,14] Auger recombination,[21,22] and exciton redistribution/diffusion,[5,14,26] would give insight into further tunability and control of these systems' optical and spintronic properties.[27−29] Recent experimental results characterizing the photoluminescence dynamics[5,14,26] in these systems inspires state-of-the-art simulations. In this study, we explore nonradiative relaxation processes in a variety of SWCNT chiralities and single-defect functionalization chemistries to elucidate the structure-dependent tunability of the exciton relaxation into the energetically low-lying emitting state associated with the defect.

SWCNT chirality and chemical species used for functionalization affect the optoelectronic characteristics of the material. As such, we constructed a set of SWCNTs with differing chiralities—(6,2), (6,5), (9,1), (11,0), and (7,6)—and resulting differing diameters (0.57, 0.75, 0.75, 0.86, and 0.88 nm) and chiral angles (14, 27, 5.2, 0, and 27.5°), respectively. The pristine (6,2) SWCNT is functionalized with

Received: August 27, 2022
Accepted: March 21, 2023
Published: March 27, 2023

https://doi.org/10.1021/acsnano.2c08579
ACS Nano 2023, 17, 6208−6219

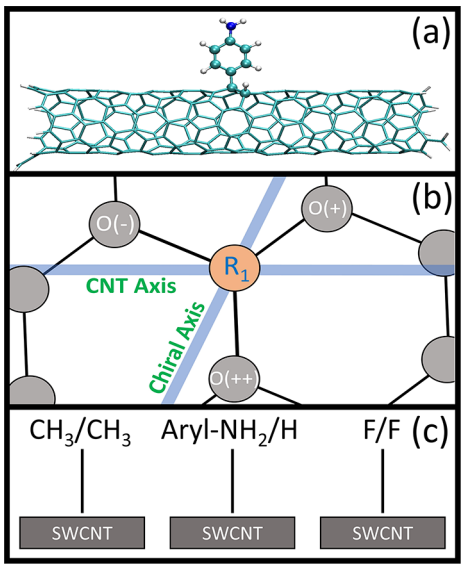

Figure 1. (a) (6,2) SWCNT with Aryl-NH_2/H defect in the *ortho*(+) configuration. (b) Definition of the defect configuration with respect to the tube and chiral axes. (c) Chemical species used as chemical adducts in this work.

a set of chemical adducts—F/F, CH_3/CH_3, Aryl-NH_2/H—focusing on the *ortho* binding configurations with opposing optical features—*ortho*(+) and *ortho*(++), where *ortho* indicates that the set of covalent attachments are bonded to adjacent carbon atoms (see Figure 1 and Methods). (6,2) was chosen for the exploration of defect species dependence due to its small diameter, which reduces the computational cost of the dynamics and an intermediate chiral angle characteristic for multiple nanotube species. From our previous studies,[2,3,7,10] the binding configuration of the defect, uniquely defined by the angle between the vector connecting the two functionalized carbon atoms and the tube axis vector, has the largest control over the emission energy. The low-lying defect state (denoted as E_{11}*) can be energetically lower than the lowest fundamental excitonic band of the nanotube E_{11} by 100−400 meV. The chosen configuration's red shift depends uniquely on the SWCNT chirality (specifically the mod (n-m,3) value).[3] Changing the functional group has a much smaller effect (10−100 meV).[1,7] We note that the charge on the sp^3-hybridized SWCNT atom connected directly to the defect and the hybridization of the bonding defect atom correlates with the amount of red shift of the defect exciton from the pristine E_{11} exciton,[1,6,7] which implies that strongly electron-withdrawing groups such as direct fluorine attachment (denoted as F/F or 2F in this work) typically provide the lowest-energy E_{11}* excitation.

Previous experimental work[5,14] has suggested that strong thermal detrapping and exciton redistribution processes are prevalent prior to emission on time scales similar to the expected nonradiative relaxation. In designing ideal quantum

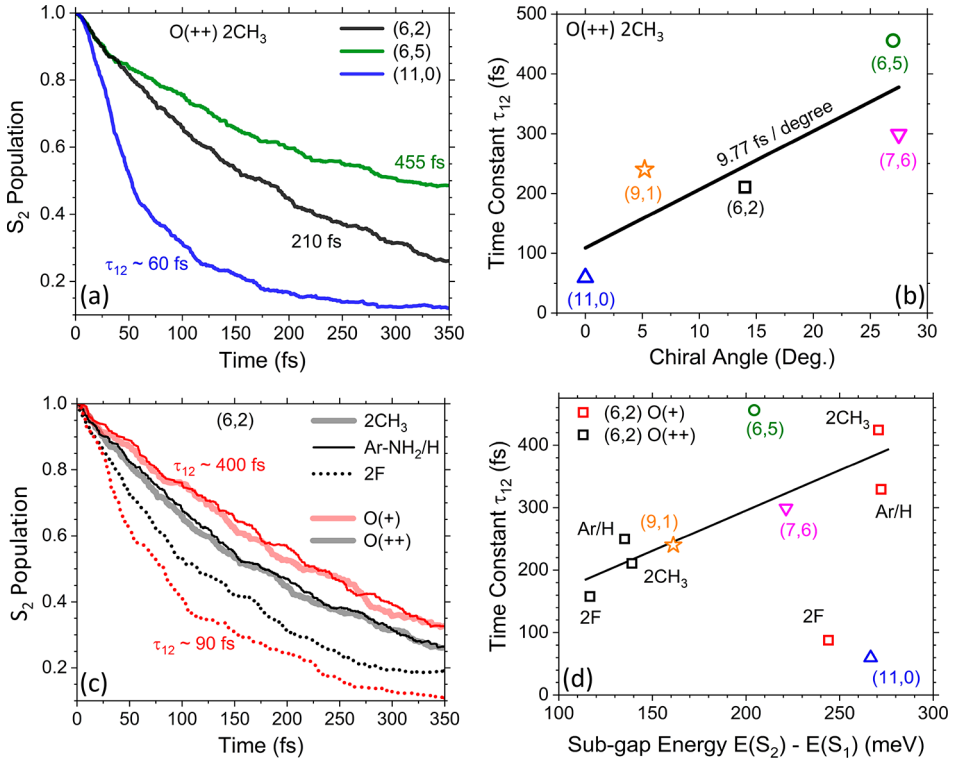

Figure 2. (a) Population dynamics for a set of SWCNT chiralities ((6,2), (11,0), and (6,5)) and two defect configurations for the (6,2) chirality (*ortho*(+) and *ortho*(++)). (b) Dependence of the relaxation time constant τ_{12}, given by a single-exponential fit to the explicit nonadiabatic trajectory surface hopping dynamics, on the chiral angle of the various SWCNT species. The results of an additional two chiralities (9,1) (orange star) and (7,6) (pink inverted triangle) are shown, also with *ortho*(++) 2CH_3 defect schemes. The data were fit to a line with slope 9.77 fs/deg. (c) Chemical composition dependence in the (6,2) chirality with 2CH_3 (bold line), Aryl-NH_2/H (solid line), and 2F (dotted line) as chemical adducts. (d) Dependence of the relaxation time constant τ_{12} on the subgap energy between electronic states S_1 and S_2 evaluated at the ground-state minimum geometry. The solid line indicates the trend in relaxation time constants for the (6,2) SWCNT (red and black symbols) and is simply a guide for the eye to show the "gap-law" trend in the nonfluorinated defect compositions.

https://doi.org/10.1021/acsnano.2c08579
ACS Nano 2023, 17, 6208−6219

emitters with useful properties—such as small spectral line widths and large energetic separation between the lowest emitting excited state S_1 and higher electronic levels—dynamic control of the nonradiative relaxation into the S_1 state is fundamentally required. In this work, we show that such control is possible through choice of SWCNT chirality as well as defect configuration and chemical composition by a modulation of the excitonic relaxation rate from the E_{11} band-edge state to the low-lying E_{11}^* (S_1) exciton. Our results showcase a tunable single-exponential decay constant τ_{12} that varies from 60 to 450 fs through experimentally simple changes to the SWCNT chirality and functional group chemistry, where the changes in population dynamics are shown to stem from strong changes in nonadiabatic coupling and local charge distributions throughout the trajectories.

RESULTS AND DISCUSSION

The nonadiabatic excited-state molecular dynamics (NEXMD) software package[30,31] (open-source distribution available at https://github.com/lanl/NEXMD) has been used for all simulations presented in this work, and computational methodology is presented in Methods. Briefly, after performing Born−Oppenheimer dynamics at room temperature to produce conformational samples of the geometry in the ground state, we initialized a set of nonadiabatic trajectories in the second singlet electronic excited state S_2, which, for the cases of (6,2) and (11,0), possesses the character/energy of the E_{11} band-edge exciton and, for example, (6,5) does not, but it is still used for the initial state due to fast relaxation from higher electronic states. See Figures S1−S3 in the Supporting Information for absorption spectra with additional discussion on the validity of the semiempirical calculations, Figures S4−S6 for natural transition orbitals of pristine and defected models, and Figure S7 for a brief discussion on higher excited states and the S_2-to-S_1 rate-limiting step for the (6,5) SWCNT. The nuclear and electronic degrees of freedom (DOFs) were propagated in time according to the trajectory surface hopping (TSH) method[32] as implemented in NEXMD with excitonic effects considered at the configuration interaction singles (CIS) level. This trajectory-based method uses the rigorous excited-state potential energy surfaces and samples all vibrational modes of the system through the so-called "on-the-fly" approach. In particular, this necessarily includes nuclear modes stemming from the crystalline backbone as well as the defect-localized modes. By virtue of the on-the-fly dynamics, anharmonic effects are explicitly included through the motion of the nuclear DOFs.

The goal of the present work is to examine the dynamics of the exciton after all large-scale dynamics have occurred (including diffusion and trapping/detrapping processes), or more specifically, once the exciton has been "captured" by the defect and intends to relax downward through the excited-state manifold governed by the local structure of the defect site. This would account for only the last stage in the overall vibronic relaxation process(es) found in experiment, just before the radiative photoluminescence process occurs. The size of our SWCNT atomistic model prohibits the inclusion of these large-scale processes and is expected to be a focus of future theoretical studies. Our hope is that the results presented here will inspire the community at large to develop new experiments focused on the defect-associated relaxation dynamics as a probe of chemical functionalization and encourage new theoretical works aimed at large-scale on-the-fly dynamics with similar methodologies to extend the time and length scales of the simulation.

The excited-state population was computed at each time step and averaged across 300 trajectories for each system to evaluate relaxation rates by fitting the S_2 population to a single exponential $P_2(t) \approx e^{-t/\tau_{12}}$ (Figure 2a; see Figure S8 in the Supporting Information for convergence with number of trajectories and Figure S9 in the Supporting Information for a discussion on length-dependent results). A strong dependence on chirality (Figure 2a) is seen among the (11,0), (6,2), and (6,5) SWCNTs with increasing single-exponential relaxation time τ_{12} = 60, 210, and 455 fs, respectively, where these systems were functionalized with $2CH_3$ in the Ortho(++) configuration. This choice of functional species was explored in previous studies[1,7,12] and provides a functional species that should have a minimal impact on the SWCNT aside from the sp^3 hybridization, in contrast to other types of defects which may have large charge induction, such as 2F, as will be explored later.

The trend in chirality cannot be attributed to diameter, since (6,2) has the smallest diameter, followed by (6,5) and (11,0). The chiral angle is the dominating factor, since the zigzag (11,0) relaxes much more quickly than the chiral (6,5) and (6,2). Figure 2b shows the relaxation time constant as a function of the chiral angle for the already discussed (11,0), (6,2), and (6,5) models as well as two additional chiralities (9,1) and (7,6), also with *ortho*(++) $2CH_3$ defects. (9,1) and (7,6) observed relaxation times of τ_{12} = 240 and 299 fs, respectively, lying between the other chiralities. A linear fit explicitly demonstrates the dependence of the relaxation time on the chiral angle with an approximate slope of 9.77 fs/deg. Since (11,0) provides a comparatively fast relaxation from the higher-energy states to a quasi-two-state subsystem {S_0, S_1}, we suggest its use in quantum light-emitting applications to minimize thermal detrapping events.

Focusing on the (6,2) chirality, Figure 2c showcases the dependence of the population dynamics on the defect configuration (*ortho*(++), black; *ortho*(+), red) and composition (thick solid, $2CH_3$; thin solid, Aryl-NH_2/H; dotted, 2F). For (6,2), the *ortho*(+) configuration produces the largest red shift ($\Delta E_{11} = E_{11} - E_{11}^*$) of the S_1 defect-associated state from the pristine band-edge exciton E_{11} (see Figures S1−S3 in the Supporting Information) and *ortho*(++) system the second largest, yet small, which is consistent with our previous work.[3] In this sense, the decay constant τ_{12} is expected to be dependent on the electronic energy differences between excited states dictated by the configuration (i.e., nonradiative "gap law").[33] For the $2CH_3$ (Aryl-NH_2/H) adduct, *ortho*(++) and *ortho*(+) configurations produce single-exponential decay times of τ_{12} = 210 (250) and 424 (330) fs, respectively. As expected for the configuration with the larger red shift, the relaxation time is longer since the energetic gap is increased; however, for the 2F adduct, this trend is broken with decay times of 158 and 88 fs for *ortho*(++) and *ortho*(+), respectively. We elucidate this abnormality later.

For the (6,2) chirality (red and black squares in Figure 2d), the gap-law trend (black line) holds for the methyl and aryl adducts, but the fluorinated cases act oppositely. The (6,5) (circle), (11,0) (triangle), (9,1) (star), and (7,6) (inverted triangle) chiralities are expected to act independently (i.e., with unique gap-law prefactors) from the (6,2) due to the differences in diameter and mod(*n*-*m*,3) values.[3] One would need to explore various configurations and chemical

https://doi.org/10.1021/acsnano.2c08579
ACS Nano 2023, 17, 6208−6219

compositions of defects on these SWCNTs to find a reasonable gap law involving these structures. Throughout the rest of this study, we focus our attention on the (11,0), (6,5), and (6,2) chiralities, since all further conclusions can be easily generalized to all chiralities.

Out of context, these characteristic relaxation times discussed above may seem to be disconnected from experimental findings. For example, in recent experimental reports[14,34] studying the relaxation times of covalently functionalized SWCNTs, the reported relaxation times were given in terms of a biexponential decay. The short-time ($\sim 10^1$ ps) characteristic relaxation constants (τ_S) were attributed to the exciton redistribution across bright and dark defect-associated states, while the long-time ($\sim 10^2$ ps) relaxation constants (τ_L) were attributed to the relaxation to the ground state. Due to limited computational resources, our calculations cannot be extended to the interesting physical processes at long time scales such as (I) exciton diffusion, (II) S_1-to-S_0 nonadiabatic relaxations, or (III) optical transition rates. However, our simulations do give direct insight into the short-time constant from experiment, which explicitly includes the exciton relaxation and redistribution processes at the defect site.[14] Notably, and in contrast to previous reports,[34] we find that the excitonic relaxation after the diffusion process has occurred is largely modified by the choice of defect composition. In fact, for a high concentration of defects, our change in relaxation time could modify the experimentally found short-time constant by up to 10%,[34] given the tunability we report in this paper of up to 0.5 ps during the final part of the relaxation process to the low-energy E_{11}* state.

The probability of hopping between adiabatic states is dictated by the magnitude of the scalar nonadiabatic coupling terms (NACT; see Methods), so that systems that sample large NACT magnitudes more frequently may exhibit faster population decay. Figure 3 shows the probability distributions of the NACT *at the moment of a hop* from the S_2 to S_1 state for each system with unique population dynamics (omitting aryl adducts, since they show trends similar to those of methyl). Examining the (6,2) structures (Figure 3a,b), the configuration of the defect shows varied distributions, with *ortho*(++) exhibiting a much longer tail than *ortho*(+), even for the $2CH_3$ adduct (black). The long tail in the NACT should be correlated with sampling larger NACT on average and thus gives rise to faster nonradiative decay. In both configurations, the average NACT (vertical dotted lines) for the 2F (red) adduct is larger than the $2CH_3$. For the (6,5) (black) and (11,0) (red), with the two extremum population decay rates, the average NACT follows the expected trend.

The NACT distributions for the fluorinated cases suggest that the *ortho*(++) may relax faster due to the long tail; however, we find the opposite (Figure 2c), in contrast to the $2CH_3$ case. As such, we seek to understand the physical mechanism that controls the NACT throughout the trajectory in each system. To answer these questions, we turn our attention to various dynamic quantities that may relate the chemistry of the system (i.e., charge, bond character, etc.) to the corresponding NACT quantity and population decay.

Previous experimental and theoretical reports have substantiated the importance of the electrostatic effects of the electron-withdrawing groups attached to the SWCNT surface. In the static picture (i.e., at the Condon geometry), recent theoretical investigations have revealed that the electronegativity of the functional species systematically red-shifts

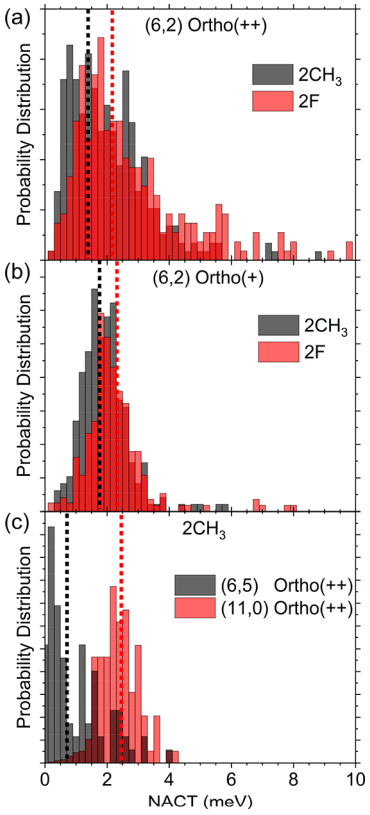

Figure 3. Probability distributions for the magnitude of the scalar nonadiabatic coupling terms (NACT) at a moment of hop from S_2 to S_1. (6,2) systems with (a) *ortho*(++) and (b) *ortho*(+), each with $2CH_3$ (black) and 2F (red). (c) (6,5) (black) and (11,0) (red), each with $2CH_3$ in their respective *ortho*(++). The vertical dashed lines indicate the mean value of the distribution.

the primary defect-associated emission feature, E_{11}*.[1,7] This was also seen in experiment and correlated to the Hammett substituent constant (i.e., a quantitative measure of the electronegativity of the functional species).[6,35−38] These electrostatic effects cause a large degree of perturbation to the local charges on the tube surface near the defect attachment. This is believed to dictate the subtle red shift stemming from chemical composition of the defect; however, we posit that this redistribution of local charges drastically affects the relaxation rate through known changes to the hybridization of the SWCNT carbon atoms bonded to the defect, ultimately causing the coupling between electronic wave functions of the states.

Figure 4 shows the probability distributions of four useful quantities necessary for the chemical interpretation of the nonadiabatic dynamics. The natural bond orbital (NBO) bond character (depicted as % s) and NBO charge of the SWCNT-defect interfacial atoms were extracted from the NAMD trajectories. Note that all systems are of (6,2) chirality. The % s character on the SWCNT atom (Figure 4a) with the 2F adduct restricts the values to near 21−23%, while the $2CH_3$ adducts—having a more flexible bond—allow the s character to fluctuate widely between 20 and 29%. Note that 33% indicates an sp^2 carbon. The *ortho*(++) (black) distribution is centered at 25% (i.e., sp^3), while the *ortho*(+) (green) shows a bimodal nature with centers at 22 and 27%. Since all species show overlapping distributions, the % s character on the SWCNT atom may not be a reliable indicator of the population decay properties

https://doi.org/10.1021/acsnano.2c08579
ACS Nano 2023, 17, 6208−6219

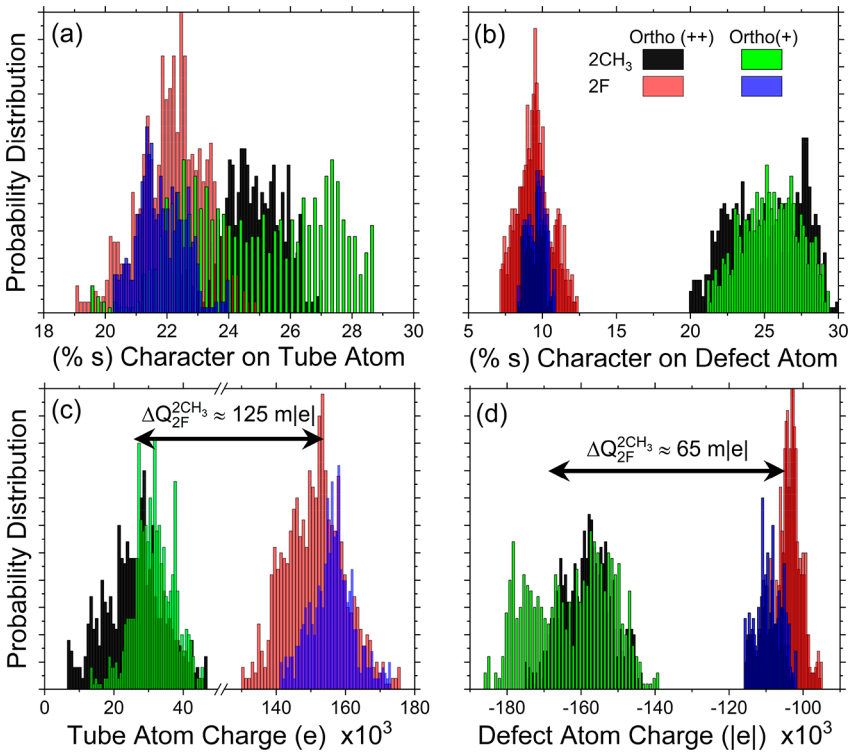

Figure 4. Probability distributions for the (a) percent s-atomic orbital character (% s) on the SWCNT atom attached to the defect, (b) % s character on the defect atom connected to the SWCNT, (c) NBO charge on the SWCNT atom, and (d) NBO charge on the defect atom. All systems have (6,2) chirality.

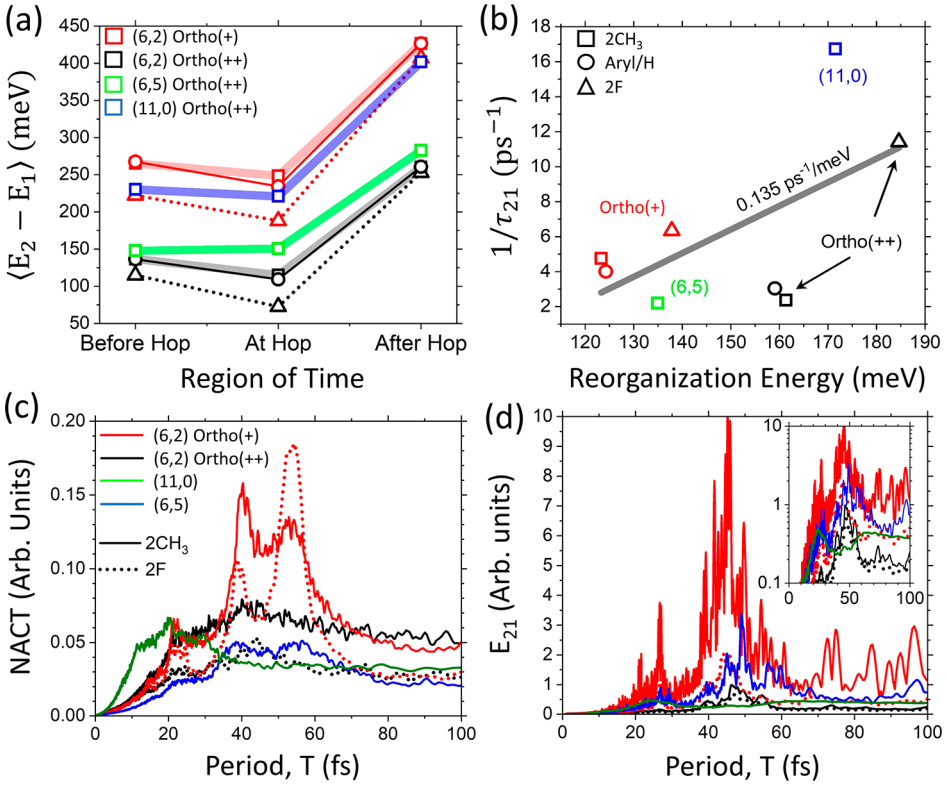

Figure 5. (a) Subgap energy $E_2 - E_1$ as an average over time and trajectory taken before the hop (while in S_2), at the hop (only trajectory average), and after the hop (while in S_1). (b) Rate of population transfer from S_2 to S_1 ($1/\tau_{21}$) as a function of reorganization energy at finite temperature E_R between S_2 and S_1 calculated as $E_R = \langle E_{21}^{After} \rangle - \langle E_{21}^{Before} \rangle$, where $\langle ... \rangle$ denote time and trajectory averages. A linear fit was performed on all data points, indicating a slope of 0.135 ± 0.07 ps^{-1}/meV. Frequency distributions for two dynamical quantities: (c) scalar nonadiabatic coupling terms (NACT) and (d) subgap energy $E_2 - E_1$.

https://doi.org/10.1021/acsnano.2c08579
ACS Nano 2023, 17, 6208−6219

between similar defect types (i.e., methyl or aryl); however, the 2F adducts decrease the % s character. Generally, bonds involving atoms with higher p character are less rigid, since unhybridized p orbitals generate more rigid bonds due to increased p orbital overlap. The higher p character in the 2F system therefore may influence the most active vibrational modes, resulting in the increased relaxation rate. The % s character on the defect atom (covalently bonded to the SWCNT atom, Figure 4b) shows nonoverlapping distributions between C and F attachments. This indicates that the C-adduct bonds are fluctuating around sp^3 hybridization (% s ~25%), while the F-adduct bonds are dominated by p atomic orbitals with contributions of up to 90% p. This property of the adduct atom is not likely to directly influence the relaxation rate, since the exciton is not spatially localized onto the adduct. Figure 4c,d shows the NBO charge on the SWCNT atom and defect atom.

As noted previously, the charge on the SWCNT atom has been suggested to control the emission energy of the defect state (E_{11}*). To be clear, here we are not interested in the radiative transition energy between E_{11}* and the ground state; rather, we are interested in the nonradiative transition between E_{11} and E_{11}*, which has not yet been correlated to the SWCNT charge. The charge on the SWCNT atom (Figure 4c) is positive in both types of adducts, as was shown in a previous report,[7] but the probability distributions at finite temperature for both configurations are slightly shifted by ~10 millielectrons (mlel) from one another; the *ortho*(++) configuration shows a smaller positive charge on the SWCNT atom. Moving to the charge on the defect atom (Figure 4d), we find the opposite—but equivalent—effect, where the charge on the defect atom in the *ortho*(++) configuration shows a slightly smaller negative charge (~10 mlel). We note that the charge on the defect atom in the $2CH_3$ *ortho*(+) case is again showing a bimodal distribution with centers at −180 and −155 mlel, similar to the % s character on the SWCNT atom for the same species. This bimodal nature may be indicative of a large nuclear reorganization between the E_{11} and E_{11}* electronic states, which will be the main point of the following discussion. The probability distributions of the subgap energy $E_2 - E_1$ are shown in Figure S10 for the (6,2) chirality, which shows information similar to that for Figure 2d.

Nuclear reorganization upon electronic excitation is generally assumed to be small in rigid systems like SWCNTs[39,40] and therefore not considered as a main driving force for nonradiative decay to lower excited states. However, our calculations show that the reorganization energy between S_2 (E_{11}) and S_1 (E_{11}*) is on the order of 150 meV, on the same order as the red shift of the defect-associated state from the band edge. Figure 5a shows the S_2/S_1 subgap energy averaged over time and trajectory *before*, *at*, and *after* the transition to the lower S_1 state for all species. Notably, at the transition, all species except (6,5) (which has the smallest reorganization energy) show a decrease in subgap energy, implying that the thermal fluctuations in the state energies allow for increased NACT ≈ $1/E_{21}$ (see Figure S11 for subgap energy dependence on the time constant before, at, and after the hop; see Figure S12 for the time- and trajectory-resolved subgap energy data). The fluorinated adducts show an increased reduction in subgap energy at the hop, which points to *increased energetic fluctuations in the fluorinated systems*. The subgap energy after the transition is noticeably higher than that before the hop, which indicates a significant reorganization energy between S_1 and S_2. Figure 5b depicts the transition rate ($1/\tau_{21}$) as a function of the reorganization energy, which is then fit to a linear function with a slope of 0.135 ± 0.07 ps^{-1}/meV. The data suggest a correlation between the relaxation rate and the reorganization energy, which can be interpreted as increased sampling of a smaller energy difference between electronically excited states due to a large shift in the excited state minimum. Similar values of E_{11}/E_{11}* thermal reorganization energies were experimentally reported for aryl-functionalized SWCNTs, near 150 meV with a linear dependence on defect concentration.[41] Interestingly, Aryl/H and $2CH_3$ share the same reorganization energy, so *the reorganization is expected to stem from the local redistribution of charges between the excited states*, governed by the strong electronegative 2F adducts, which is evident from Figure 4. The defect atoms themselves play little to no role in the reorganization (see Figure S13 for a brief analysis of the geometric reorganization). It is important to note that the choice of subgap energy does not largely affect the trends shown in Figure 2d at the Condon geometry (see Figure S11 for comparison with non-Condon geometries).

To elucidate the direct effects on the NACT, we now examine dynamic quantities in Fourier space. Figure 5c,d shows frequency (in oscillation period) distributions of various dynamical quantities (NACT, Figure 5c; subgap energy $E_2 - E_1$, Figure 5d). We note that the Fourier spectrum of the NACT shows widely varied localization properties between chiralities and adduct types. The two (6,2) *ortho*(+) species exhibit two large peaks near 40−45 and 55 fs, in addition to a weak peak near 25 fs. The last peak can be directly attributed to C−C bond stretching throughout the SWCNT lattice (see Figure S14 for a Fourier representations of C−C and C−F bond lengths, respectively), while the first two peaks at higher oscillation period show that the NACTs are more strongly coupled to some slower vibronic modes (see Figure S15 for a statistical approach to analyze the dynamic correlation between various quantities and Figure S16 for an example of simulated off-resonant Raman spectra for the pristine and defected cases). The relative heights in the two large peaks showcase the modification from the $2CH_3$ (solid, red) to the 2F (dotted, red) adducts; the fluorination shifts the peak at 40−45 fs down and the peak at 55 fs up, effectively swapping the relative contributions of the two modes. However, neither mode disappears or becomes shifted, indicating that the effects stem from the change in SWCNT bonding frequencies near the defect due to the change in the local charge distribution and resulting hybridization. This hypothesis is supported by previous work on π-orbital mismatch,[1,10] which demonstrates that the nearby bonds are deformed in such a way as to produce an increased mismatch between adjacent π-orbitals. This effect would also manifest itself in the resulting vibrational modes localized near the defect.

The subgap energy (Figure 5d) for the (6,2) *ortho*(+) (red) shows characteristics in Fourier space similar to that of the NACT, which is expected since NACT ≈ $1/\Delta E$, although with additional noise for the $2CH_3$ adduct especially. The dominant peak is found at 45−50 fs with a second near 55−60 fs. The inset shows a vertical log scale. All species also exhibit a small peak near the 20 fs mode. For the NACT, the most similar to the two (6,2) *ortho*(+) species (red) is the (11,0) chirality (blue), although it shows much weaker coupling to the two modes. In contrast, the two (6,2) *ortho*(++) species show significant delocalization across the Fourier space, exhibiting a very weak peak at around 40−45 fs. In this case, the peak at 55

https://doi.org/10.1021/acsnano.2c08579
ACS Nano 2023, 17, 6208−6219

fs disappears completely for both the $2CH_3$ and 2F adducts, indicating that the change in configuration decoupled the NACT from the higher-period mode. Strangely, the (6,5) SWCNT contains only a single peak at 20 fs. All species have a small peak at this frequency, which is expected to stem from the carbon backbone of the SWCNT (Figure S12a). The subgap energy for (6,5) (Figure 5d) also only couples to the 20 fs mode, while the other chiralities show significant peaks at around 20 and 45 fs. All other species couple to the same two modes as in the NACT. These data indicate that the (6,5) chirality provides NACT values that are decoupled from both main modes seen in other functionalized SWCNT chiralities, supporting its slow population dynamics.

CONCLUSIONS

We have explored the effects of topological sp^3 defects on the nonradiative relaxation dynamics in SWCNT systems between the band-edge E_{11} and defect-associated E_{11}* excitons. Utilizing semiempirical simulations that have been well justified in similar systems[31,42,43] and at the configuration interaction (CIS) level accounting for electrostatically bound excitonic effects, SWCNTs of more than 500 atoms were modeled. While many experimental works have explored similar physics at the sub-ps time scale,[5,8,14,15,44−65] the conclusions found in this study will have broad impacts on both the quantum dynamics and SWCNT communities. We have rooted out the structure−property correspondence between the defect's chemical composition and topological configuration as well as between SWCNT chiralities. To our surprise, the chemical composition of the sp^3 defect was largely responsible for the resulting population relaxation rate, showing that the electronegative fluorine adducts cause a large redistribution of charges near the defect site compared to that of methyl adducts. As such, all properties controlling the relaxation (i.e., the nonadiabatic couplings) are modified.

In a recent report, we have discussed that one can achieve a reasonably large tunability in red shift purely from the chemical composition of the defect in only the most red-shifted configuration.[7] However, for the dynamic situation presented here, it seems that the composition of the defect plays a larger role in determining the excitonic relaxation than its configuration, in stark contrast to expectations. This is an extremely relevant finding that showcases an important instance where one needs move past the "static picture" for these systems in order to rationalize experimental results on time-resolved excitonic dynamics.

It should be noted that the time constants produced here are not directly comparable to the biexponential decay fits of recent works,[5,14] as the systems in this work are extremely short (2−3 nm) and exhibit only a single defect-associated state below the E_{11} exciton. However, the information stored in the time constants here can be interpreted qualitatively as a measure of the electronic coupling between the bright emitting state E_{11}* and the higher-energy E_{11} in experiment, which gives information on the relaxation dynamics. This information is vital to adapt these systems for use in spintronic applications—where our results suggest that functionalizing low-chiral angle SWCNTs with strongly electronic withdrawing groups such as 2F provide quick decay into the quasi-two-state subsystem $\{S_0, S_1\}$.

Further, our data suggest that the reorganization energy between excited states is large due to the charge redistribution on the surface. Subsequently, this factor needs to be accounted for in modeling approaches to properly describe dynamics on the excited-state potential energy surfaces and excited-state coherence and dephasing phenomena that can affect nonradiative relaxation of an electronic excitation.

The broad results of these nonadiabatic simulations have a direct impact on new experimental studies investigating spatially local dynamics near a defect site, such as those important for thermal trapping/detrapping events as well as exciton redistribution processes in the defect-associated manifold of topologically rich, low-energy states. Indeed, the absolute values of the current numerical study are not quantitatively comparable to those of experiments for generally reported photoluminescence dynamics, where the time constants include such processes as exciton diffusion along the SWCNT; however, the objective trends between chiralities and defect composition have a clear physical insight from the chiral angle as well as the varied local charge distribution between defect chemistries, respectively. We believe that this work can inspire experimental studies into the intrinsic dynamics near the defect sites, which contain a complicated and interesting potential energy surface for the excitons, even for small concentrations of defects. Additionally, performing molecular simulations such as these often leads to many interesting and unexpected results stemming from the unique structure of the system in highly nontrivial fashions. Future theoretical studies can be attempted with larger SWCNT systems that are aimed at encapsulating longer time-scale experimental phenomena like exciton diffusion processes or explicit defect−defect interactions.

Thus, this work shows that direct atomistic nonadiabatic dynamics simulations deliver important insights into excitonic dynamics of chemically functionalized carbon nanotubes. In our future studies, we will address (I) the effects of various normal modes on the reorganization energy to elucidate the important contributions from the geometric rearrangement between excited states, (II) the effects of π-orbital mismatch on the nonadiabatic coupling, (III) excitonic localization and its time-dependent correlations with the nonadiabatic coupling, and (IV) interacting defect systems to showcase dynamic motion of the exciton between the coupled, deep potential energy wells.

METHODS

The open-source NEXMD package provides a reliable framework to explore the previously unexplorable nonadiabatic dynamics in the basis of excitons (at the CIS or RPA level) rather than independent electron/hole picture on systems involving hundreds of atoms. In addition, one has the freedom to explore various Hamiltonians, such as AM1, PM6, DFTB, etc., and solvent models for the ground and excited states, such as linear response, state-specific, and vertical excitation. The electronic DOFs are evolved using the FSSH approach with options to include instantaneous decoherence as well as algorithms for evaluating instances of unavoided crossings. All methods are performed utilizing analytical gradients for fast propagation of the nuclei (i.e., adiabatic state gradients) as well as the electronic subsystems (i.e., nonadiabatic couplings).

Quantum-Chemical Methodology. Using the semiempirical Austin Model I (AM1) Hamiltonian (see Scheme S1 in the Supporting Information),[66] which has been utilized to carry out otherwise computationally unfeasible quantum dynamics simulations on many organic molecules,[31,67−70] the ground-state single-particle density matrix

$$(\rho)_{nm} = \langle 0|\hat{c}_n^{\dagger}\hat{c}_m|0\rangle \quad (1)$$

https://doi.org/10.1021/acsnano.2c08579
ACS Nano 2023, 17, 6208−6219

is solved self-consistently, where $|0\rangle$ is the adiabatic electronic ground state of the system and $\hat{c}_n^\dagger$ ($\hat{c}_n$) is the creation (annihilation) operator for atomic orbital n. The collective electronic oscillator (CEO) method[71−73] was used to provide solutions to the linearized time-dependent Hartree−Fock (TD-HF) equations of motion for the single-particle transition density matrix

$$(\xi_\alpha)_{nm} = \langle 0|\hat{c}_n^\dagger \hat{c}_m|\alpha\rangle \tag{2}$$

in the configuration interaction singles (CIS) approximation, which neglects the de-excitation contributions

$$\hat{A}\xi_\alpha = \Omega_\alpha \xi_\alpha \tag{3}$$

where $\{|\alpha\rangle\}$ are the excited adiabatic electronic states, $\hat{A}$ is the CIS matrix, and Ω_α are the electronic transition energies with respect to the ground state self-consistent field (SCF) energy E_0: $E_\alpha = E_0 + \Omega_\alpha$.

Quantum-Classical Electronic Propagation. Trajectory-based, mixed quantum-classical methods have been explored in great depth over the last few decades and used to simulate a variety of molecular species and solid-state materials.[32,68,74−89] Tully's fewest switches surface hopping (FSSH) method[32] was used to propagate the electronic degrees of freedom (DOF) nonadiabatically using *ad hoc* decoherence corrections[90] along with trivial avoided crossing routines.[91]

The electronic part of the wave function can be expanded in the basis of adiabatic states $\{|\alpha\rangle\}$

$$|\Psi(\mathbf{R}(t))\rangle = \sum_\alpha c_\alpha(t)|\alpha(\mathbf{R}(t))\rangle \tag{4}$$

where c_α are time-dependent expansion coefficients for the adiabatic basis and $\mathbf{R}$ represents the nuclear configuration. Using the time-dependent Schrödinger equation (TDSE), one obtains the equation of motion for these coefficients

$$\dot{c}_j = -ic_j E_j - \sum_k c_k \dot{\vec{R}}\cdot\vec{d}_{jk} \tag{5}$$

where $\hbar = 1$ and $\vec{d}_{jk} = \langle j\left|\overrightarrow{\nabla_R}\right|k\rangle = \langle j|\frac{\partial \hat{H}_{el}}{\partial \vec{R}}|k\rangle/(E_j - E_k)$ are the vectoral nonadiabatic coupling (NACR) matrix elements with the symmetry property $\vec{d}_{jk} = -\vec{d}_{kj}$ and $\vec{d}_{kk} = \vec{0}$. A commonly used simplification is to derive the nonadiabatic coupling directly from the time dependence of the nuclear propagation.[92] Using the chain rule, one obtains the scalar nonadiabatic coupling terms (NACT), $\langle j\left|\frac{\partial}{\partial t}\right|k\rangle = \dot{\vec{R}}\cdot\vec{d}_{jk}$, which can be obtained by finite difference methods during the nuclear propagation or analytically. By default, the NEXMD package[30] computes the NACT and NACR analytically as

$$\vec{d}_{jk} = \frac{\mathrm{Tr}\left[\frac{\partial F_{jk}}{\partial \vec{R}}\rho_{jk}\right]}{\Omega_j - \Omega_k} \tag{6}$$

$$\dot{\vec{R}}\cdot\vec{d}_{jk} = \frac{\mathrm{Tr}\left[\frac{\partial F_{jk}}{\partial t}\rho_{jk}\right]}{\Omega_j - \Omega_k} \tag{7}$$

where F_{jk} are the Fock matrix elements and $\rho_{jk} = c_j^* c_k$ is the reduced electronic density matrix, respectively. The probability that the electronic state will hop from adiabatic state j to state k during the nuclear time step Δt is given by

$$g_{jk} = \Delta t \frac{b_{jk}(t)}{\rho_{jj}(t)} \tag{8}$$

where $b_{jk}(t) = -2\mathrm{Re}[\rho_{kj}^* \dot{\vec{R}}\cdot\vec{d}_{jk}]$, $g_{jk} = -g_{kj}$, and $g_{kk} = 0$. At each nuclear step, the value of g_{jk} is compared to a uniformly distributed random number $\chi \in [0,1]$, and a hop from j to k is performed if

$$\sum_{\gamma=1}^{k} g_{j\gamma} < \chi < \sum_{\gamma=1}^{k+1} g_{j\gamma} \tag{9}$$

where the adiabatic states are assumed to be ordered by increasing energy. No hop is performed if either $\sum_{\gamma=1}^{N_s} g_{j\gamma} < \chi < 1$ or $g_{jk} < 0$, where N_s is the number of included adiabatic states. In this work, N_s = 2 (includes S_1 and S_2 in electronic dynamics but includes up to S_3 in the CIS determination of the excited states), which may introduce errors involving the lack of coherence between higher states, but we expect this to be small due to the large subgap between S_2 and S_3 in these systems and will only change the relaxation of the population to a small degree, leaving the qualitative trends unchanged. If a hop is probabilistically accepted, an attempt is made to rescale the nuclear kinetic energy in the direction of the NACR (which are only necessarily computed at nuclear steps that satisfy eq 9) in order to conserve the total energy of the system.[92,93] Otherwise, the hop is rejected and denoted as a frustrated hop.

Since the adiabatic expansion coefficients are quickly varying in time and the NACT may become highly peaked in regions of large nonadiabaticity (e.g., at conical intersections), the electronic subsystem is integrated with a time step $\delta t = \Delta t/N_{el}$, where N_{el} is the number of electronic steps per nuclear time step. At each electronic step, eq 5 is integrated via the fifth-order Runge−Kutta method by separating the real and imaginary parts into coupled first-order-in-time differential equations.[68] The nuclei are propagated classically via the symplectic and time-reversible velocity-Verlet integration scheme using the analytical gradients of the active adiabatic state k to obtain the nuclear forces, $\vec{F} = -\nabla V_k$, where V_k is the kth eigenvalue of the electronic Hamiltonian at the present nuclear configuration. In this work, the nuclear time step was set to Δt = 0.25 fs with N_{el} = 4 electronic time steps per nuclear step. To acquire the proper initial sampling of nuclear degrees of freedom (DOFs), each system was thermalized in the canonical ensemble (also called the fixed NVT ensemble)—defined as fixing the following set of macroscopic variables: number of atoms/electrons N, volume V, and temperature T—in the electronic ground state for 10 ps. Excluding the first 100 fs (for purposes of equilibration), the initial nuclear positions and momenta for the 300 nonadiabatic excited state dynamics trajectories were taken from the remaining 9.9 ps of ground-state dynamics to appropriately sample the ground state distribution, taking snapshots (i.e., initial phase space configurations) roughly every 33 fs.

The transition density matrix at each nuclear step contains an arbitrary global phase, which is tracked between time steps and corrected such that the following identity is enforced, $\langle\xi_j|\xi_k\rangle = \mathrm{Tr}[\rho_{00}[\xi_j^\dagger \xi_k]] = \delta_{jk}$, where δ_{jk} is the Kronecker delta.[30]

Trivial unavoided crossings are a known drawback of the FSSH method, and with any finite-sized nuclear time step, the hopping probability may be underestimated. Unavoided crossings are checked between each nuclear time step, and a hop between noninteracting adiabatic states is performed in order to continue evolving along the diabatic state if a crossing is found.[91]

The instantaneous decoherence correction (IDC) scheme was utilized to recover the decoherence of the wavepacket in an empirical way, since the standard FSSH approach fails to give accurate results for the coherences in the reduced electronic density matrix. The IDC scheme is implemented such that at each hop (or frustrated hop), the expansion coefficients are reset such that the active state—the resulting state after a hop or the original state in the case of a frustrated hop—is set to unity, while the others are set to zero. Between hops, the coefficients are allowed to evolve normally by eq 5, allowing the wavepacket to broaden naturally. This procedure[90] allows an instantaneous decoherence correction to occur after the branching of a wavepacket from one state to the next, where the two pieces of the wavepacket are now largely decoupled.

Solvent effects were included through the linear response formalism.[68,94−96] Often, for large systems, including solvent effects allows for easier convergence of the ground-state SCF algorithm. The

https://doi.org/10.1021/acsnano.2c08579
ACS Nano 2023, 17, 6208−6219

linear response correction is generally poor for nonadiabatic dynamics in systems where differences in permanent dipole moments in the ground and excited states are large, but we note in our SWCNT systems, the permanent dipoles are largely equivalent between states due to the rigidity of the systems.

Three chiralities of SWCNTs were explored: (6,2), (6,5), and (11,0) (see Table S1). The (6,2) SWCNT was constructed with two unit cells (~3 nm in length) using the Visual Molecular Dynamics package[97] and contains 236 atoms after applying the proper capping scheme to recover the delocalized electronic structure of SWCNTs, as shown in our previous work.[98,99] The (6,5) and (11,0) tubes were constructed similarly with one (~4 nm) and 7 (~3 nm) unit cells and 394 and 354 atoms after capping, respectively. A single defect—the formation of two covalent bonds while breaking the conjugation of two SWCNT carbon atoms—was placed at the center of each SWCNT using different chemical species. There are six (four) unique configurations for any chiral (zigzag) SWCNT.[3] We denote the main and auxiliary groups of each defect as R_1/R_2. For (6,2), the chemical species explored were F/F (or 2F), CH_3/CH_3 (or $2CH_3$), and Aryl-NH_2/H. For (6,5) and (11,0), only $2CH_3$ was explored and only in the *ortho*(++) configuration.

ASSOCIATED CONTENT

Data Availability Statement

This work was published previously on the ChemRxiv preprint server: Braden M. Weight, Andrew E. Sifain, Brendan J. Gifford, Han Htoon, and Sergei Tretiak. On-the-fly Nonadiabatic Dynamics Simulations of Single-Walled Carbon Nanotubes with Covalent Defects. 2022. ChemRxiv. 10.26434/chemrxiv-2022-chjjw (accessed March 10, 2023).

Supporting Information

The Supporting Information is available free of charge at https://pubs.acs.org/doi/10.1021/acsnano.2c08579.

Convergence of the dynamics, figures that aid in the explanation of the main points, and all SWCNT ground-state optimized geometries in XYZ format (PDF)

AUTHOR INFORMATION

Corresponding Author

Sergei Tretiak − *Center for Integrated Nanotechnologies, Center for Nonlinear Studies, and Theoretical Division, Los Alamos National Laboratory, Los Alamos, New Mexico 87545, United States;* orcid.org/0000-0001-5547-3647; Email: serg@lanl.gov

Authors

Braden M. Weight − *Department of Physics and Astronomy, University of Rochester, Rochester, New York 14627, United States; Center for Integrated Nanotechnologies, Center for Nonlinear Studies, and Theoretical Division, Los Alamos National Laboratory, Los Alamos, New Mexico 87545, United States;* orcid.org/0000-0002-2441-3569

Andrew E. Sifain − *Department of Chemistry, Princeton University, Princeton, New Jersey 08540, United States;* orcid.org/0000-0002-2964-1923

Brendan J. Gifford − *Center for Integrated Nanotechnologies, Center for Nonlinear Studies, and Theoretical Division, Los Alamos National Laboratory, Los Alamos, New Mexico 87545, United States;* orcid.org/0000-0002-4116-711X

Han Htoon − *Center for Integrated Nanotechnologies, Center for Nonlinear Studies, and Theoretical Division, Los Alamos National Laboratory, Los Alamos, New Mexico 87545, United States;* orcid.org/0000-0003-3696-2896

Complete contact information is available at: https://pubs.acs.org/10.1021/acsnano.2c08579

Notes

The authors declare no competing financial interest.

ACKNOWLEDGMENTS

This work was performed in part at the Center for Integrated Nanotechnology (CINT) and Center for Nonlinear Studies (CNLS), U.S. Department of Energy and Office of Basic Energy Sciences user facilities and supported by the Los Alamos National Laboratory (LANL) Directed Research and Development funds (LDRD). For computational resources, the authors thank the Center for Integrated Research Computing (CIRC) at the University of Rochester as well as the LANL Institutional Computing for providing computational resources and technical support.

REFERENCES

(1) Gifford, B. J.; He, X.; Kim, M.; Kwon, H.; Saha, A.; Sifain, A. E.; Wang, Y.; Htoon, H.; Kilina, S.; Doorn, S. K.; Tretiak, S. Optical Effects of Divalent Functionalization of Carbon Nanotubes. *Chem. Mater.* **2019**, *31* (17), 6950−6961.

(2) Gifford, B. J.; Kilina, S.; Htoon, H.; Doorn, S. K.; Tretiak, S. Exciton Localization and Optical Emission in Aryl-Functionalized Carbon Nanotubes. *J. Phys. Chem. C* **2018**, *122* (3), 1828−1838.

(3) Gifford, B. J.; Saha, A.; Weight, B. M.; He, X.; Ao, G.; Zheng, M.; Htoon, H.; Kilina, S.; Doorn, S. K.; Tretiak, S. Mod(n-m,3) Dependence of Defect-State Emission Bands in Aryl-Functionalized Carbon Nanotubes. *Nano Lett.* **2019**, *19* (12), 8503−8509.

(4) He, X.; Gifford, B. J.; Hartmann, N. F.; Ihly, R.; Ma, X.; Kilina, S. V.; Luo, Y.; Shayan, K.; Strauf, S.; Blackburn, J. L.; Tretiak, S.; Doorn, S. K.; Htoon, H. Low-Temperature Single Carbon Nanotube Spectroscopy of Sp ^{3} Quantum Defects. *ACS Nano* **2017**, *11* (11), 10785−10796.

(5) He, X.; Sun, L.; Gifford, B. J.; Tretiak, S.; Piryatinski, A.; Li, X.; Htoon, H.; Doorn, S. K. Intrinsic Limits of Defect-State Photoluminescence Dynamics in Functionalized Carbon Nanotubes. *Nanoscale* **2019**, *11* (18), 9125−9132.

(6) Kwon, H.; Furmanchuk, A.; Kim, M.; Meany, B.; Guo, Y.; Schatz, G. C.; Wang, Y. Molecularly Tunable Fluorescent Quantum Defects. *J. Am. Chem. Soc.* **2016**, *138* (21), 6878−6885.

(7) Weight, B. M.; Gifford, B. J.; Tretiak, S.; Kilina, S. Interplay between Electrostatic Properties of Molecular Adducts and Their Positions at Carbon Nanotubes. *J. Phys. Chem. C* **2021**, *125* (8), 4785−4793.

(8) Settele, S.; Berger, F. J.; Lindenthal, S.; Zhao, S.; El Yumin, A. A.; Zorn, N. F.; Asyuda, A.; Zharnikov, M.; Högele, A.; Zaumseil, J. Synthetic Control over the Binding Configuration of Luminescent Sp 3 -Defects in Single-Walled Carbon Nanotubes. *Nat. Commun.* **2021**, *12* (1), 2119.

(9) Lohmann, S.-H.; Trerayapiwat, K. J.; Niklas, J.; Poluektov, O. G.; Sharifzadeh, S.; Ma, X. Sp3-Functionalization of Single-Walled Carbon Nanotubes Creates Localized Spins. *ACS Nano* **2020**, *14* (12), 17675−17682.

(10) Gifford, B. J.; Kilina, S.; Htoon, H.; Doorn, S. K.; Tretiak, S. Controlling Defect-State Photophysics in Covalently Functionalized Single-Walled Carbon Nanotubes. *Acc. Chem. Res.* **2020**, *53* (9), 1791−1801.

(11) Kilina, S.; Ramirez, J.; Tretiak, S. Brightening of the Lowest Exciton in Carbon Nanotubes via Chemical Functionalization. *Nano Lett.* **2012**, *12* (5), 2306−2312.

(12) Weight, B. M.; Sifain, A. E.; Gifford, B. J.; Kilin, D.; Kilina, S.; Tretiak, S. Coupling between Emissive Defects on Carbon Nanotubes: Modeling Insights. *J. Phys. Chem. Lett.* **2021**, *12* (32), 7846−7853.

(13) Zheng, Y.; Bachilo, S. M.; Weisman, R. B. Controlled Patterning of Carbon Nanotube Energy Levels by Covalent DNA Functionalization. *ACS Nano* **2019**, *13* (7), 8222−8228.
(14) Zheng, Y.; Weight, B. M.; Jones, A. C.; Chandrasekaran, V.; Gifford, B. J.; Tretiak, S.; Doorn, S. K.; Htoon, H. Photoluminescence Dynamics Defined by Exciton Trapping Potential of Coupled Defect States in DNA-Functionalized Carbon Nanotubes. *ACS Nano* **2021**, *15* (1), 923−933.
(15) Zheng, Y.; Kim, Y.; Jones, A. C.; Olinger, G.; Bittner, E. R.; Bachilo, S. M.; Doorn, S. K.; Weisman, R. B.; Piryatinski, A.; Htoon, H. Quantum Light Emission from Coupled Defect States in DNA-Functionalized Carbon Nanotubes. *ACS Nano* **2021**, *15* (6), 10406−10414.
(16) Endo, T.; Ishi-Hayase, J.; Maki, H. Photon Antibunching in Single-Walled Carbon Nanotubes at Telecommunication Wavelengths and Room Temperature. *Appl. Phys. Lett.* **2015**, *106* (11), 113106.
(17) Jeantet, A.; Chassagneux, Y.; Raynaud, C.; Roussignol, Ph.; Lauret, J. S.; Besga, B.; Estève, J.; Reichel, J.; Voisin, C. Widely Tunable Single-Photon Source from a Carbon Nanotube in the Purcell Regime. *Phys. Rev. Lett.* **2016**, *116* (24), 247402.
(18) Weight, B. M.; Zheng, M.; Tretiak, S. Signatures of Chemical Dopants in Simulated Resonance Raman Spectroscopy of Carbon Nanotubes. *J. Phys. Chem. Lett.* **2023**, *14* (5), 1182−1191.
(19) Kryjevski, A.; Mihaylov, D.; Kilina, S.; Kilin, D. Multiple Exciton Generation in Chiral Carbon Nanotubes: Density Functional Theory Based Computation. *J. Chem. Phys.* **2017**, *147* (15), 154106.
(20) Kryjevski, A.; Gifford, B.; Kilina, S.; Kilin, D. Theoretical Predictions on Efficiency of Bi-Exciton Formation and Dissociation in Chiral Carbon Nanotubes. *J. Chem. Phys.* **2016**, *145* (15), 154112.
(21) Hyeon-Deuk, K.; Prezhdo, O. V. Time-Domain Ab Initio Study of Auger and Phonon-Assisted Auger Processes in a Semiconductor Quantum Dot. *Nano Lett.* **2011**, *11* (4), 1845−1850.
(22) Pal, S.; Casanova, D.; Prezhdo, O. V. Effect of Aspect Ratio on Multiparticle Auger Recombination in Single-Walled Carbon Nanotubes: Time Domain Atomistic Simulation. *Nano Lett.* **2018**, *18* (1), 58−63.
(23) Lüer, L.; Hoseinkhani, S.; Polli, D.; Crochet, J.; Hertel, T.; Lanzani, G. Size and Mobility of Excitons in (6, 5) Carbon Nanotubes. *Nature Phys.* **2009**, *5* (1), 54−58.
(24) Perebeinos, V.; Tersoff, J.; Avouris, P. Mobility in Semiconducting Carbon Nanotubes at Finite Carrier Density. *Nano Lett.* **2006**, *6* (2), 205−208.
(25) Postupna, O.; Jaeger, H. M.; Prezhdo, O. V. Photoinduced Dynamics in Carbon Nanotube Aggregates Steered by Dark Excitons. *J. Phys. Chem. Lett.* **2014**, *5* (21), 3872−3877.
(26) Amori, A. R.; Hou, Z.; Krauss, T. D. Excitons in Single-Walled Carbon Nanotubes and Their Dynamics. *Annu. Rev. Phys. Chem.* **2018**, *69* (1), 81−99.
(27) Laird, E. A.; Pei, F.; Kouwenhoven, L. P. A Valley-Spin Qubit in a Carbon Nanotube. *Nat. Nanotechnol.* **2013**, *8* (8), 565−568.
(28) Cubaynes, T.; Delbecq, M. R.; Dartiailh, M. C.; Assouly, R.; Desjardins, M. M.; Contamin, L. C.; Bruhat, L. E.; Leghtas, Z.; Mallet, F.; Cottet, A.; Kontos, T. Highly Coherent Spin States in Carbon Nanotubes Coupled to Cavity Photons. *npj Quantum Information* **2019**, *5* (1), 1−5.
(29) Piao, Y.; Meany, B.; Powell, L. R.; Valley, N.; Kwon, H.; Schatz, G. C.; Wang, Y. Brightening of Carbon Nanotube Photoluminescence through the Incorporation of Sp 3 Defects. *Nat. Chem.* **2013**, *5* (10), 840−845.
(30) Malone, W.; Nebgen, B.; White, A.; Zhang, Y.; Song, H.; Bjorgaard, J. A.; Sifain, A. E.; Rodriguez-Hernandez, B.; Freixas, V. M.; Fernandez-Alberti, S.; Roitberg, A. E.; Nelson, T. R.; Tretiak, S. NEXMD Software Package for Nonadiabatic Excited State Molecular Dynamics Simulations. *J. Chem. Theory Comput.* **2020**, *16* (9), 5771−5783.
(31) Sifain, A. E.; Bjorgaard, J. A.; Nelson, T. R.; Nebgen, B. T.; White, A. J.; Gifford, B. J.; Gao, D. W.; Prezhdo, O. V.; Fernandez-Alberti, S.; Roitberg, A. E.; Tretiak, S. Photoexcited Nonadiabatic Dynamics of Solvated Push-Pull π-Conjugated Oligomers with the NEXMD Software. *J. Chem. Theory Comput.* **2018**, *14* (8), 3955−3966.
(32) Tully, J. C. Molecular Dynamics with Electronic Transitions. *J. Chem. Phys.* **1990**, *93* (2), 1061−1071.
(33) Englman, R.; Jortner, J. The Energy Gap Law for Radiationless Transitions in Large Molecules. *Mol. Phys.* **1970**, *18* (2), 145−164.
(34) Hartmann, N. F.; Velizhanin, K. A.; Haroz, E. H.; Kim, M.; Ma, X.; Wang, Y.; Htoon, H.; Doorn, S. K. Photoluminescence Dynamics of Aryl Sp3 Defect States in Single-Walled Carbon Nanotubes. *ACS Nano* **2016**, *10* (9), 8355−8365.
(35) Shiraki, T.; Uchimura, S.; Shiraishi, T.; Onitsuka, H.; Nakashima, N. Near Infrared Photoluminescence Modulation by Defect Site Design Using Aryl Isomers in Locally Functionalized Single-Walled Carbon Nanotubes. *Chem. Commun.* **2017**, *53* (93), 12544−12547.
(36) Shiraki, T.; Shiga, T.; Shiraishi, T.; Onitsuka, H.; Nakashima, N.; Fujigaya, T. Multistep Wavelength Switching of Near-Infrared Photoluminescence Driven by Chemical Reactions at Local Doped Sites of Single-Walled Carbon Nanotubes. *Chem. - Eur. J.* **2018**, *24* (72), 19162−19165.
(37) Shiraki, T.; Onitsuka, H.; Shiraishi, T.; Nakashima, N. Near Infrared Photoluminescence Modulation of Single-Walled Carbon Nanotubes Based on a Molecular Recognition Approach. *Chem. Commun.* **2016**, *52* (88), 12972−12975.
(38) Shiraishi, T.; Shiraki, T.; Nakashima, N. Substituent Effects on the Redox States of Locally Functionalized Single-Walled Carbon Nanotubes Revealed by in Situ Photoluminescence Spectroelectrochemistry. *Nanoscale* **2017**, *9* (43), 16900−16907.
(39) Shreve, A. P.; Haroz, E. H.; Bachilo, S. M.; Weisman, R. B.; Tretiak, S.; Kilina, S.; Doorn, S. K. Determination of Exciton-Phonon Coupling Elements in Single-Walled Carbon Nanotubes by Raman Overtone Analysis. *Phys. Rev. Lett.* **2007**, *98* (3), 037405.
(40) Yin, Y.; Vamivakas, A. N.; Walsh, A. G.; Cronin, S. B.; Ünlü, M. S.; Goldberg, B. B.; Swan, A. K. Optical Determination of Electron-Phonon Coupling in Carbon Nanotubes. *Phys. Rev. Lett.* **2007**, *98* (3), 037404.
(41) Kim, M.; Adamska, L.; Hartmann, N. F.; Kwon, H.; Liu, J.; Velizhanin, K. A.; Piao, Y.; Powell, L. R.; Meany, B.; Doorn, S. K.; Tretiak, S.; Wang, Y. Fluorescent Carbon Nanotube Defects Manifest Substantial Vibrational Reorganization. *J. Phys. Chem. C* **2016**, *120* (20), 11268−11276.
(42) Dreuw, A.; Head-Gordon, M. Single-Reference Ab Initio Methods for the Calculation of Excited States of Large Molecules. *Chem. Rev.* **2005**, *105* (11), 4009−4037.
(43) Ondarse-Alvarez, D.; Nelson, T.; Lupton, J. M.; Tretiak, S.; Fernandez-Alberti, S. Let Digons Be Bygones: The Fate of Excitons in Curved π-Systems. *J. Phys. Chem. Lett.* **2018**, *9* (24), 7123−7129.
(44) Kozawa, D.; Wu, X.; Ishii, A.; Fortner, J.; Otsuka, K.; Xiang, R.; Inoue, T.; Maruyama, S.; Wang, Y.; Kato, Y. K. Formation of Organic Color Centers in Air-Suspended Carbon Nanotubes Using Vapor-Phase Reaction. *Nat. Commun.* **2022**, *13* (1), 2814.
(45) Niidome, Y.; Yu, B.; Juhasz, G.; Fujigaya, T.; Shiraki, T. Structure Dependence of Photoluminescence Solvatochromic Energy Shifts Based on Exciton Localization in Locally Functionalized Single-Walled Carbon Nanotubes. *J. Phys. Chem. C* **2021**, *125* (23), 12758−12766.
(46) Ackermann, J.; Metternich, J. T.; Herbertz, S.; Kruss, S. Biosensing with Fluorescent Carbon Nanotubes. *Angew. Chem., Int. Ed.* **2022**, *61* (18), No. e202112372.
(47) Janas, D. Perfectly Imperfect: A Review of Chemical Tools for Exciton Engineering in Single-Walled Carbon Nanotubes. *Materials Horizons* **2020**, *7* (11), 2860−2881.
(48) Berger, F. J.; Lüttgens, J.; Nowack, T.; Kutsch, T.; Lindenthal, S.; Kistner, L.; Müller, C. C.; Bongartz, L. M.; Lumsargis, V. A.; Zakharko, Y.; Zaumseil, J. Brightening of Long, Polymer-Wrapped Carbon Nanotubes by Sp3 Functionalization in Organic Solvents. *ACS Nano* **2019**, *13* (8), 9259−9269.

https://doi.org/10.1021/acsnano.2c08579
ACS Nano 2023, 17, 6208−6219

(49) Berger, F. J.; de Sousa, J. A.; Zhao, S.; Zorn, N. F.; El Yumin, A. A.; Quintana García, A.; Settele, S.; Högele, A.; Crivillers, N.; Zaumseil, J. Interaction of Luminescent Defects in Carbon Nanotubes with Covalently Attached Stable Organic Radicals. *ACS Nano* **2021**, *15* (3), 5147−5157.
(50) Lüttgens, J. M.; Berger, F. J.; Zaumseil, J. Population of Exciton-Polaritons via Luminescent Sp3 Defects in Single-Walled Carbon Nanotubes. *ACS Photonics* **2021**, *8* (1), 182−193.
(51) Zorn, N. F.; Berger, F. J.; Zaumseil, J. Charge Transport in and Electroluminescence from Sp3-Functionalized Carbon Nanotube Networks. *ACS Nano* **2021**, *15* (6), 10451−10463.
(52) Spreinat, A.; Dohmen, M. M.; Lüttgens, J.; Herrmann, N.; Klepzig, L. F.; Nißler, R.; Weber, S.; Mann, F. A.; Lauth, J.; Kruss, S. Quantum Defects in Fluorescent Carbon Nanotubes for Sensing and Mechanistic Studies. *J. Phys. Chem. C* **2021**, *125* (33), 18341−18351.
(53) Zaumseil, J. Luminescent Defects in Single-Walled Carbon Nanotubes for Applications. *Advanced Optical Materials* **2022**, *10* (2), 2101576.
(54) Shiraki, T. Molecular Functionalization of Carbon Nanotubes towards Near Infrared Photoluminescent Nanomaterials. *Chem. Lett.* **2021**, *50* (3), 397−404.
(55) Hou, Z.; Tumiel, T. M.; Krauss, T. D. Spatially Resolved Photoluminescence Brightening in Individual Single-Walled Carbon Nanotubes. *J. Appl. Phys.* **2021**, *129* (1), 014305.
(56) Zhou, G.; Cen, C.; Wang, S.; Deng, M.; Prezhdo, O. V. Electron-Phonon Scattering Is Much Weaker in Carbon Nanotubes than in Graphene Nanoribbons. *J. Phys. Chem. Lett.* **2019**, *10* (22), 7179−7187.
(57) Godin, A. G.; Setaro, A.; Gandil, M.; Haag, R.; Adeli, M.; Reich, S.; Cognet, L. Photoswitchable Single-Walled Carbon Nanotubes for Super-Resolution Microscopy in the near-Infrared. *Science Advances* **2019**, *5* (9), No. eaax1166.
(58) Danné, N.; Kim, M.; Godin, A. G.; Kwon, H.; Gao, Z.; Wu, X.; Hartmann, N. F.; Doorn, S. K.; Lounis, B.; Wang, Y.; Cognet, L. Ultrashort Carbon Nanotubes That Fluoresce Brightly in the Near-Infrared. *ACS Nano* **2018**, *12* (6), 6059−6065.
(59) Kawabe, R.; Takaki, H.; Ibi, T.; Maeda, Y.; Nakagawa, K.; Maki, H. Pure and Efficient Single-Photon Sources by Shortening and Functionalizing Air-Suspended Carbon Nanotubes. *ACS Appl. Nano Mater.* **2020**, *3* (1), 682−690.
(60) Chen, Y.; Marty, L.; Bendiab, N. New Light on Molecule-Nanotube Hybrids. *Adv. Mater.* **2019**, *31* (48), 1902917.
(61) Kim, Y.; Velizhanin, K. A.; He, X.; Sarpkaya, I.; Yomogida, Y.; Tanaka, T.; Kataura, H.; Doorn, S. K.; Htoon, H. Photoluminescence Intensity Fluctuations and Temperature-Dependent Decay Dynamics of Individual Carbon Nanotube Sp3 Defects. *J. Phys. Chem. Lett.* **2019**, *10* (6), 1423−1430.
(62) He, X.; Velizhanin, K. A.; Bullard, G.; Bai, Y.; Olivier, J.-H.; Hartmann, N. F.; Gifford, B. J.; Kilina, S.; Tretiak, S.; Htoon, H.; Therien, M. J.; Doorn, S. K. Solvent- and Wavelength-Dependent Photoluminescence Relaxation Dynamics of Carbon Nanotube Sp3 Defect States. *ACS Nano* **2018**, *12* (8), 8060−8070.
(63) He, X.; Gifford, B. J.; Hartmann, N. F.; Ihly, R.; Ma, X.; Kilina, S. V.; Luo, Y.; Shayan, K.; Strauf, S.; Blackburn, J. L.; Tretiak, S.; Doorn, S. K.; Htoon, H. Low-Temperature Single Carbon Nanotube Spectroscopy of Sp ^{3} Quantum Defects. *ACS Nano* **2017**, *11* (11), 10785−10796.
(64) Kwon, H.; Kim, M.; Nutz, M.; Hartmann, N. F.; Perrin, V.; Meany, B.; Hofmann, M. S.; Clark, C. W.; Htoon, H.; Doorn, S. K.; Högele, A.; Wang, Y. Probing Trions at Chemically Tailored Trapping Defects. *ACS Cent. Sci.* **2019**, *5* (11), 1786−1794.
(65) Zheng, W.; Zorn, N. F.; Bonn, M.; Zaumseil, J.; Wang, H. I. Probing Carrier Dynamics in Sp3-Functionalized Single-Walled Carbon Nanotubes with Time-Resolved Terahertz Spectroscopy. *ACS Nano* **2022**, *16* (6), 9401−9409.
(66) Dewar, M. J. S.; Zoebisch, E. G.; Healy, E. F.; Stewart, J. J. P. Development and Use of Quantum Mechanical Molecular Models. 76. AM1: A New General Purpose Quantum Mechanical Molecular Model. *J. Am. Chem. Soc.* **1985**, *107* (13), 3902−3909.
(67) Nelson, T. R.; Ondarse-Alvarez, D.; Oldani, N.; Rodriguez-Hernandez, B.; Alfonso-Hernandez, L.; Galindo, J. F.; Kleiman, V. D.; Fernandez-Alberti, S.; Roitberg, A. E.; Tretiak, S. Coherent Exciton-Vibrational Dynamics and Energy Transfer in Conjugated Organics. *Nat. Commun.* **2018**, *9* (1), 2316.
(68) Nelson, T. R.; White, A. J.; Bjorgaard, J. A.; Sifain, A. E.; Zhang, Y.; Nebgen, B.; Fernandez-Alberti, S.; Mozyrsky, D.; Roitberg, A. E.; Tretiak, S. Non-Adiabatic Excited-State Molecular Dynamics: Theory and Applications for Modeling Photophysics in Extended Molecular Materials. *Chem. Rev.* **2020**, *120* (4), 2215−2287.
(69) Nelson, T.; Bjorgaard, J.; Greenfield, M.; Bolme, C.; Brown, K.; McGrane, S.; Scharff, R. J.; Tretiak, S. Ultrafast Photodissociation Dynamics of Nitromethane. *J. Phys. Chem. A* **2016**, *120* (4), 519−526.
(70) Sifain, A. E.; Gifford, B. J.; Gao, D. W.; Lystrom, L.; Nelson, T. R.; Tretiak, S. NEXMD Modeling of Photoisomerization Dynamics of 4-Styrylquinoline. *J. Phys. Chem. A* **2018**, *122* (49), 9403−9411.
(71) Tretiak, S.; Mukamel, S. Density Matrix Analysis and Simulation of Electronic Excitations in Conjugated and Aggregated Molecules. *Chem. Rev.* **2002**, *102* (9), 3171−3212.
(72) Hartmann, M.; Chernyak, V.; Mukamel, S. Real-Space Coupled-Oscillator Approach to the Radiative Decay of Conjugated Polymers. *Phys. Rev. B* **1995**, *52* (4), 2528−2538.
(73) Mukamel, S.; Tretiak, S.; Wagersreiter, T.; Chernyak, V. Electronic Coherence and Collective Optical Excitations of Conjugated Molecules. *Science* **1997**, *277* (5327), 781−787.
(74) Cotton, S. J.; Miller, W. H. Symmetrical Windowing for Quantum States in Quasi-Classical Trajectory Simulations: Application to Electronically Non-Adiabatic Processes. *J. Chem. Phys.* **2013**, *139* (23), 234112.
(75) Cotton, S. J.; Miller, W. H. Symmetrical Windowing for Quantum States in Quasi-Classical Trajectory Simulations. *J. Phys. Chem. A* **2013**, *117* (32), 7190−7194.
(76) Huo, P.; Coker, D. F. Communication: Partial Linearized Density Matrix Dynamics for Dissipative, Non-Adiabatic Quantum Evolution. *J. Chem. Phys.* **2011**, *135* (20), 201101.
(77) Weight, B. M.; Mandal, A.; Huo, P. Ab Initio Symmetric Quasi-Classical Approach to Investigate Molecular Tully Models. *J. Chem. Phys.* **2021**, *155* (8), 084106.
(78) Meyer, H.; Miller, W. H. A Classical Analog for Electronic Degrees of Freedom in Nonadiabatic Collision Processes. *J. Chem. Phys.* **1979**, *70* (7), 3214−3223.
(79) Stock, G.; Thoss, M. Semiclassical Description of Nonadiabatic Quantum Dynamics. *Phys. Rev. Lett.* **1997**, *78* (4), 578−581.
(80) Mannouch, J. R.; Richardson, J. O. A Partially Linearized Spin-Mapping Approach for Nonadiabatic Dynamics. I. Derivation of the Theory. *J. Chem. Phys.* **2020**, *153* (19), 194109.
(81) Runeson, J. E.; Richardson, J. O. Spin-Mapping Approach for Nonadiabatic Molecular Dynamics. *J. Chem. Phys.* **2019**, *151* (4), 044119.
(82) Curchod, B. F. E.; Martínez, T. J. Ab Initio Nonadiabatic Quantum Molecular Dynamics. *Chem. Rev.* **2018**, *118* (7), 3305−3336.
(83) Mai, S.; Marquetand, P.; González, L. Nonadiabatic Dynamics: The SHARC Approach. *WIREs Computational Molecular Science* **2018**, *8* (6), No. e1370.
(84) Crespo-Otero, R.; Barbatti, M. Recent Advances and Perspectives on Nonadiabatic Mixed Quantum-Classical Dynamics. *Chem. Rev.* **2018**, *118* (15), 7026−7068.
(85) Oloyede, P.; Mil'nikov, G.; Nakamura, H. Generalized Trajectory Surface Hopping Method Based on the Zhu-Nakamura Theory. *J. Chem. Phys.* **2006**, *124* (14), 144110.
(86) Shu, Y.; Zhang, L.; Chen, X.; Sun, S.; Huang, Y.; Truhlar, D. G. Nonadiabatic Dynamics Algorithms with Only Potential Energies and Gradients: Curvature-Driven Coherent Switching with Decay of Mixing and Curvature-Driven Trajectory Surface Hopping. *J. Chem. Theory Comput.* **2022**, *18* (3), 1320−1328.
(87) Smith, B.; Akimov, A. V. Modeling Nonadiabatic Dynamics in Condensed Matter Materials: Some Recent Advances and Applications. *J. Phys.: Condens. Matter* **2020**, *32* (7), 073001.

https://doi.org/10.1021/acsnano.2c08579
ACS Nano 2023, 17, 6208−6219

(88) Han, Y.; Kilin, D. S. Nonradiative Relaxation Dynamics of a Cesium Lead Halide Perovskite Photovoltaic Architecture: Effect of External Electric Fields. *J. Phys. Chem. Lett.* **2020**, *11* (23), 9983−9989.
(89) Cui, P.; Jabed, M.; Vogel, D. J.; Kilina, S. Phonon-Mediated Ultrafast Hole Transfer from Photoexcited CdSe Quantum Dots to Black Dye. In *ACS Symposium Series*; Kilin, D., Kilina, S., Han, Y., Eds.; American Chemical Society: 2019; Vol. *1331*, pp 137−156.
(90) Nelson, T.; Fernandez-Alberti, S.; Roitberg, A. E.; Tretiak, S. Nonadiabatic Excited-State Molecular Dynamics: Treatment of Electronic Decoherence. *J. Chem. Phys.* **2013**, *138* (22), 224111.
(91) Fernandez-Alberti, S.; Roitberg, A. E.; Nelson, T.; Tretiak, S. Identification of Unavoided Crossings in Nonadiabatic Photoexcited Dynamics Involving Multiple Electronic States in Polyatomic Conjugated Molecules. *J. Chem. Phys.* **2012**, *137* (1), 014512.
(92) Hammes-Schiffer, S.; Tully, J. C. Proton Transfer in Solution: Molecular Dynamics with Quantum Transitions. *J. Chem. Phys.* **1994**, *101* (6), 4657−4667.
(93) Fabiano, E.; Keal, T. W.; Thiel, W. Implementation of Surface Hopping Molecular Dynamics Using Semiempirical Methods. *Chem. Phys.* **2008**, *349* (1), 334−347.
(94) Cammi, R.; Mennucci, B. Linear Response Theory for the Polarizable Continuum Model. *J. Chem. Phys.* **1999**, *110* (20), 9877−9886.
(95) Bjorgaard, J. A.; Kuzmenko, V.; Velizhanin, K. A.; Tretiak, S. Solvent Effects in Time-Dependent Self-Consistent Field Methods. I. Optical Response Calculations. *J. Chem. Phys.* **2015**, *142* (4), 044103.
(96) Scalmani, G.; Frisch, M. J.; Mennucci, B.; Tomasi, J.; Cammi, R.; Barone, V. Geometries and Properties of Excited States in the Gas Phase and in Solution: Theory and Application of a Time-Dependent Density Functional Theory Polarizable Continuum Model. *J. Chem. Phys.* **2006**, *124* (9), 094107.
(97) Humphrey, W.; Dalke, A.; Schulten, K. VMD: Visual Molecular Dynamics. *J. Mol. Graph.sol* **1996**, *14* (1), 33−38.
(98) Sharma, A.; Gifford, B. J.; Kilina, S. Tip Functionalization of Finite Single-Walled Carbon Nanotubes and Its Impact on the Ground and Excited State Electronic Structure. *J. Phys. Chem. C* **2017**, *121* (15), 8601−8612.
(99) Kilina, S.; Tretiak, S. Excitonic and Vibrational Properties of Single-Walled Semiconducting Carbon Nanotubes. *Adv. Funct. Mater.* **2007**, *17* (17), 3405−3420.

https://doi.org/10.1021/acsnano.2c08579
ACS Nano 2023, 17, 6208−6219